# Light-Harvesting Properties and Morphology of Porphyrin Nanostructures Depend on Ionic Species Inducing Aggregation

Christopher W. Leishman and Jeanne L. McHale*

Department of Chemistry, Box 644630, Washington State University, Pullman, Washington 99164, United States

Ⓢ Supporting Information

ABSTRACT: Self-assembled, excitonically coupled aggregates of 5,10,15,20-tetrakis(4-sulfonatophenyl)porphyrin (TSPP) in aqueous solutions of HCl and of the alkali chloride salts LiCl, NaCl, KCl, and CsCl were studied by absorption and resonance light scattering (RLS) spectroscopy. Aggregates deposited from these solutions were imaged by transmission electron microscopy and atomic force microscopy. In NaCl and KCl, the J band in the absorption spectrum was broadened, while in CsCl it was narrowed, as compared to aggregates in HCl. In LiCl and NaCl, the relative excitonic coherence as determined from RLS was increased as compared to aggregates in HCl, while in KCl and CsCl it was reduced.

The discrepancy between measures of coherence based on exchange narrowing in the absorption spectrum and those on RLS intensity points to morphology-dependent composite J band structures. Delocalization of excitons between nanotubular subunits of bundled aggregates appears to increase excitonic coherence. Loosening of intermonomer forces, observed as bending in the images, and possibly the inclusion of alkali and/or chloride ions within composite structures, appear to limit excitonic coherence by increasing disorder. The dependence of morphologies on counterion species can be explained, in part, by the cations' differing kosmotropic versus chaotropic ion-pairing properties and effects on water structure. The results may inform methods to tune the spatial and spectral properties of excitons in these systems.
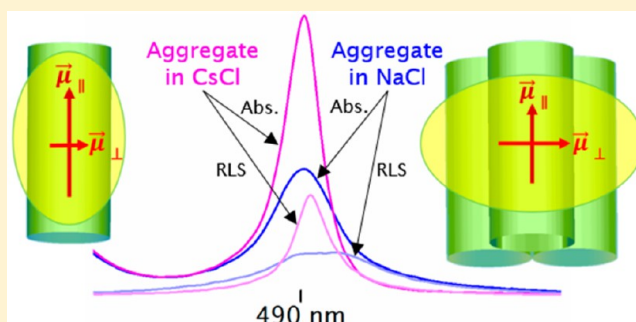
INTRODUCTION

Organic and hybrid light-harvesting materials show promise in novel photovoltaic and photocatalytic devices with plastic-like processing and mechanical characteristics as well as customizable aesthetic qualities. Nature provides inspiration for design of these materials in the pigment complexes of photosynthetic organisms, evolved to optimize efficiency while minimizing photochemical damage.[1] These structures act as quantum-coherent antennae that collect energy from sunlight and direct it to the electrochemical reaction centers.[2] In particular, the self-assembled bacteriochlorophyll nanotubes of green bacteria[3,4] exhibit variations in antenna morphology induced by the intracellular environment that enable energy transport efficiencies in excess of 90%[5] and light-harvesting into the near-infrared.[6]

Analogous artificial aggregates can be prepared from pseudoisocyanine[7] and carbocyanines,[8,9] as well as from porphyrins. In general, nanotubular aggregates display one or two major excitonic bands corresponding to the strongest monomer electronic transition, either one blue-shifted H band and one red-shifted J band, or one or two red-shifted J bands. Aggregates of some carbocyanine species can be of either spectral type depending on solvent composition,[10] while 5,10,15,20-tetrakis(4-sulfonatophenyl)porphyrin (TSPP) aggregates are of the former type under most conditions.[11,12] Because of their chemical kinship with the chlorophylls, high

symmetry of the TSPP monomer, and facile preparation in aqueous solution, TSPP aggregates are a particularly well-suited model system for exploring the structural basis of photophysical properties in excitonically coupled light-harvesting assemblies.

TSPP diacid self-aggregates in acidic aqueous solution (HCl in most studies) as a neutral zwitterionic species formed by protonation of two of the peripheral sulfonate groups of the diacid dianion monomer (Figure 1a). A satisfactory structural model of HCl-induced TSPP aggregates should have a diameter of 15−20 nm and wall width of approximately 1.5−2 nm, obtained from atomic force microscopy (AFM) and transmission electron microscopy (TEM) studies.[11,13−17] The lattice spacings and relative orientations of monomers must lead to the blue and red shifts of H and J bands observed in absorption spectra (see Figure 2d).[18,19] The major component of the J band must be polarized parallel to the tube axis and the H band perpendicular to agree with linear dichroism studies.[16,20−23] Individual aggregates should have a chiral/helical structure, in consistency with circular dichroism spectra.[20,22,23] Finally, the structure should have well-ordered domains large enough to accommodate excitons of coherence size yielding the observed
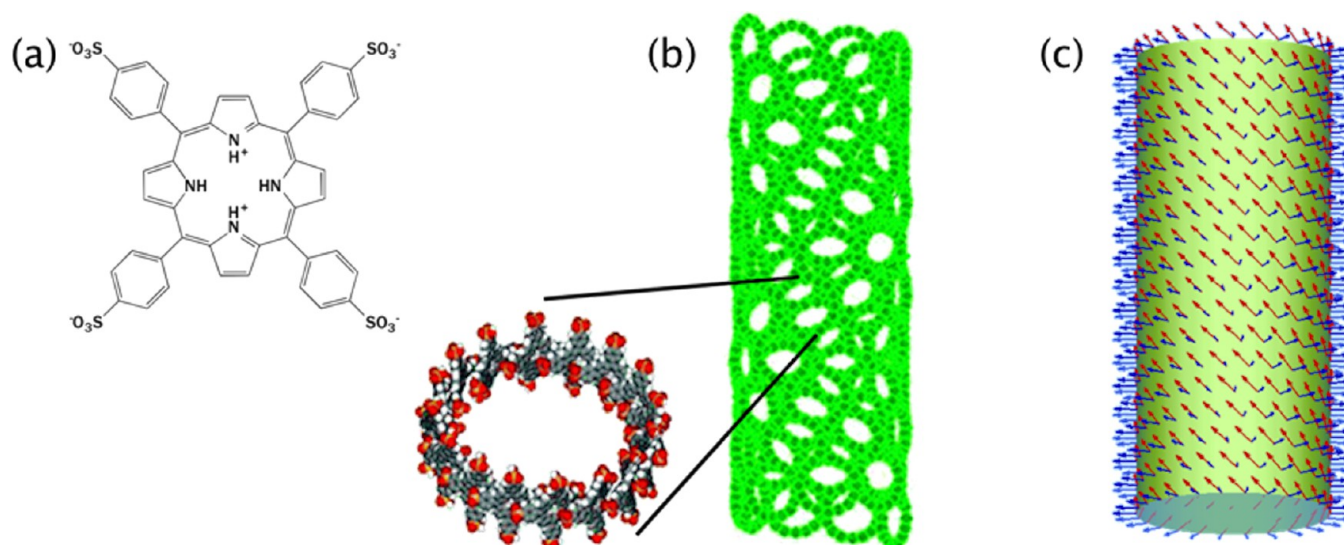
Figure 1. (a) Porphyrin diacid monomer. (b) Hierarchical helical nanotube model with cyclic 16-mer subunit (adapted from refs 7 and 11, the latter by permission of the Royal Society of Chemistry). (c) Multihelical nanotube model, drawn by the present authors, based on imaging of internal lattice in refs 13, 23, and Figure 10. Arrows correspond to monomer transition dipole moment components contributing primarily to H (blue) and J (red) bands.
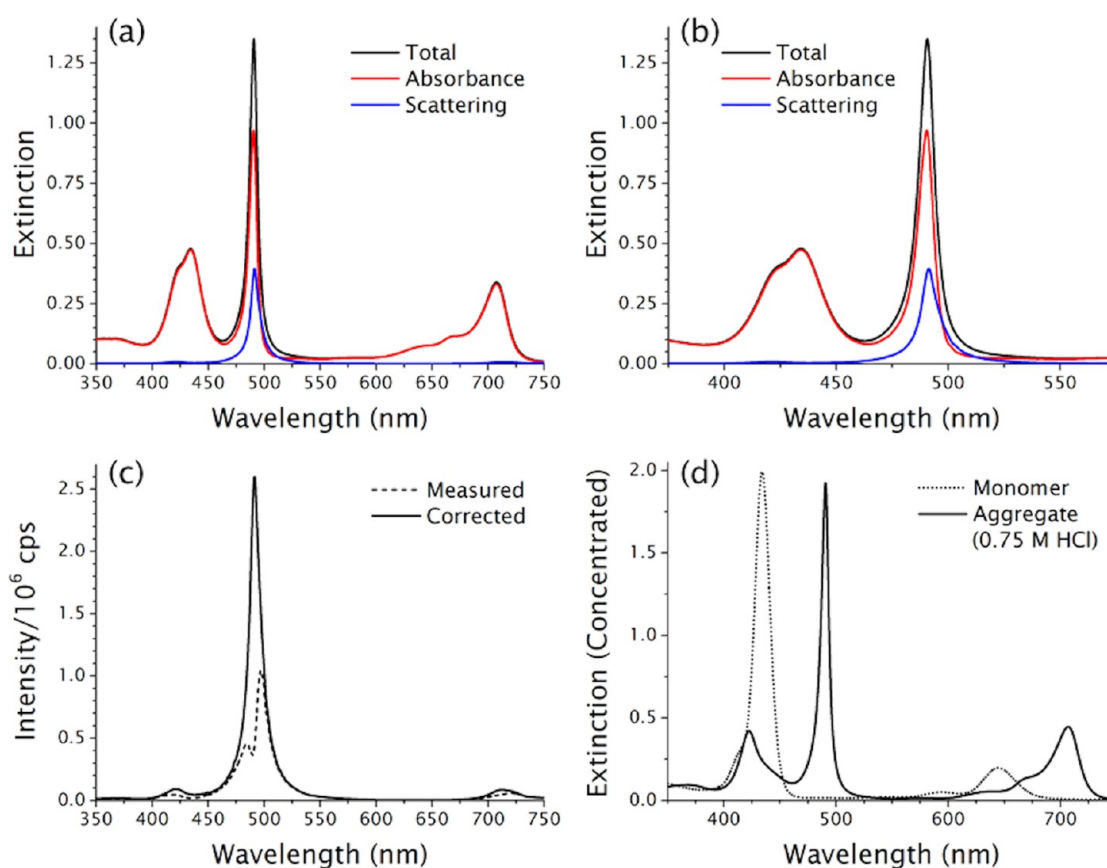
Figure 2. (a) Extinction spectra of aggregated TSPP (5 μM solution in 0.75 M aqueous HCl) showing total (black), absorbance (red), and scattering (blue) components. (b) Details of the same extinction spectra in Soret region. (c) RLS intensity of the same solution as measured (dashed line) and corrected (solid line). (d) Extinction spectra of diacid monomer (dotted line) and aggregated TSPP (50 μM in 0.75 M HCl, path length = 1 mm).

resonance light scattering (RLS) intensity and enhancement of low frequency Raman modes.[15,24−26]

Recently, we revealed resonance Raman (RR) depolarization ratio dispersion, indicative of multiple nondegenerate transitions contributing to the J band.[25] STM images showed

structures consistent with flattened tubes composed of disc-like subunits ∼6 nm in diameter.[11] A hierarchical model was proposed, with rings of ∼16 monomer units ("cyclic N-mers") arranged helically in a nanotube (Figure 1b). Here, the large splitting of the Soret band into J and H bands, along with red

shifting and enhancement of the Q bands, arises from coupling within the cyclic N-mers. Weak coupling between cyclic subunits splits the J band into components polarized parallel and perpendicular to the tube axis, consistent with RR depolarization ratio dispersion.[15,25]

This hierarchical model agrees qualitatively with all of the major spectroscopic and imaging results of which we are aware. However, regularly sized 6 nm diameter discs were observed in just a few of many STM images, among which nanotube surface features varied widely in size.[11] The disc-like features may reflect changes that occur during the deposition and drying of aggregate samples. Thus, evidence in support of the hierarchical model (nanotube of cyclic N-mers) is inconclusive. A multistart helical nanotube model (Figure 1c), consistent with cryogenic electron microscopy, diffraction data,[17] and high-resolution STM,[27] could also plausibly fit the spectroscopic results. A helical nanotube model with interwoven helices, discussed in a series of theoretical works,[16,28] may account for most of these experimental results as well. While we do not settle the matter of the internal lattice structure, we provide evidence that several different aggregation-inducing conditions lead to similar nanotubular morphologies. Also, we show one image of a structure consistent with a multistart helical nanotube.

To examine the role of water in the solution-phase aggregate structure, our group carried out isotopic substitution studies comparing aggregates in D_2O/DCl to those in H_2O/HCl.[15] Greater RLS intensity, indicating increased coherence, was seen in the deuterated as compared to the protiated environment. This was attributed to lower disorder related to smaller displacement of low-frequency modes in the excited electronic state in the deuterated species. In studies of single aggregates, relative RR intensity of low frequency versus high frequency modes decreased sharply with high-intensity laser exposure. Because the peak frequencies did not change, this effect was attributed to the disruption of water-mediated coupling between cyclic subunits, decreasing the spatial coherence responsible for J band activity.[26] These results suggested that water, hydrogen-bonded to the aggregates, significantly influences their structure and excitonic properties.

In this work, we continue our exploration of the influence of water structure by examining aggregates formed in a series of aqueous alkali halide solutions. Prior work in this vein has mainly emphasized increasing ionic strength to induce aggregation of dianionic diacid monomer (with all sulfonate groups unprotonated), with little attention to the role of counterion identity.[13,19,20,24,29,30] Here, we focus on how the identity of counterion species leads to distinct morphological and spectral properties through counterion−porphyrin pairing as well as ion-induced perturbations to the water structure.

In our group's earlier work, counterion effects were reported for aggregation of 5,10,15,20-tetrakis(4-carboxyphenyl) porphyrin (TCPP). Aqueous HCl led to toroidal structures of variable diameters (about 200−2000 nm) showing only a blue-shifted H band in the Soret region. In contrast, in HNO_3, nanorods of 3−4 nm height and several micrometer length formed, and displayed both J and H bands.[31,32] Another study found dependence of the degree of aggregation on alkali ion size in basic aqueous solution,[33] and permanent chirality has been induced by preparing aggregates in the presence of chiral counterions.[34,35] Striking effects on morphology and spectral properties (linear and nonlinear) have been induced by a number of solution and interfacial conditions involving complex intermolecular interactions.[36−42]

Hofmeister series effects and kosmotropic versus chaotropic designations of ions inform our analysis of species-dependent effects of counterions on aggregate structure. The "direct" Hofmeister series orders the alkali ions from small to large, with smaller ions inducing protein precipitation ("salting-out") and larger ions denaturing and solubilizing proteins ("salting-in").[43] The former ions are generally classified as kosmotropic ("structure-making"), while the latter are classified as chaotropic ("structure-breaking"), due to their evident effects on local water structure. In addition to the biological applications, these effects have been thoroughly investigated by physical measurements[44−46] and theoretical studies.[47−49] We will apply these concepts to the interactions of solvated cations with the porphyrin monomer to explain some of the species-dependent effects on aggregate morphology.

We survey the effects of monatomic, monovalent cations on TSPP aggregation through absorption and RLS spectra, which reveal excitonic coupling and coherence. In parallel to the spectroscopic investigations, we have directly observed features of aggregate morphologies through TEM and AFM. Here, we see the extent to which we can compare acid-induced and salt-induced aggregates and how contrasting results can instruct us about solution environment effects on morphology. Combined analysis of spectroscopic and morphological data allows us to uncover relations between cation properties and the observed variations in aggregate morphology, and to suggest a few specific relationships between morphological characteristics and optical properties.

■ EXPERIMENTAL METHODS

Sample Preparation. The dihydrochloride salt of 5,10,15,20-tetrakis(4-sulfonatophenyl)porphyrin (H_2TSPP) was purchased from Frontier Scientific Inc. (Logan, Utah) and used as received. Stock solutions of 100 or 200 μM were prepared in 18 MΩ Millipore water, and the pH was adjusted to ~3 with 1 M HCl. For 5 μM TSPP sample solutions, stock solution was first diluted to 10 μM, which was mixed 1:1 with the appropriate salt or acid solution. 1.5 M LiCl, NaCl, KCl, and CsCl stock solutions were prepared with oven-dried salts of 99% or better purity from various suppliers. Each sample was adjusted to pH ≈ 2.7 and allowed to stand for a minimum of 3 days and not longer than 5 days prior to data acquisition. This ensured consistent equilibration of the aggregation process.

UV Visible Extinction and Resonance Light Scattering Spectroscopy. UV visible extinction spectra of samples and the absorption spectrum of a nonscattering absorption standard were acquired on a Shimadzu spectrophotometer. Samples were gently vortexed prior to data acquisition to disperse flocculated aggregates.

Resonance light scattering spectra were acquired on a PTI QuantaMaster fluorimeter with xenon lamp excitation and photomultiplier tube (PMT) detection. A reference photodiode was used to correct for spectral and temporal fluctuations of lamp intensity. The excitation and emission monochromators were scanned synchronously, with sample chamber entrance and exit slits set to approximately 2.5 and 0.25 nm bandpass, respectively, for appropriate intensity levels at the reference photodiode and the PMT. Samples were stirred continuously in the sample holder during data acquisition.

Calibration for scattering in the spectrophotometer and self-absorption in the fluorimeter was performed using potassium dichromate (EMD; 1.00 mM aqueous solution) as an absorption standard and 260 nm polystyrene latex nanospheres
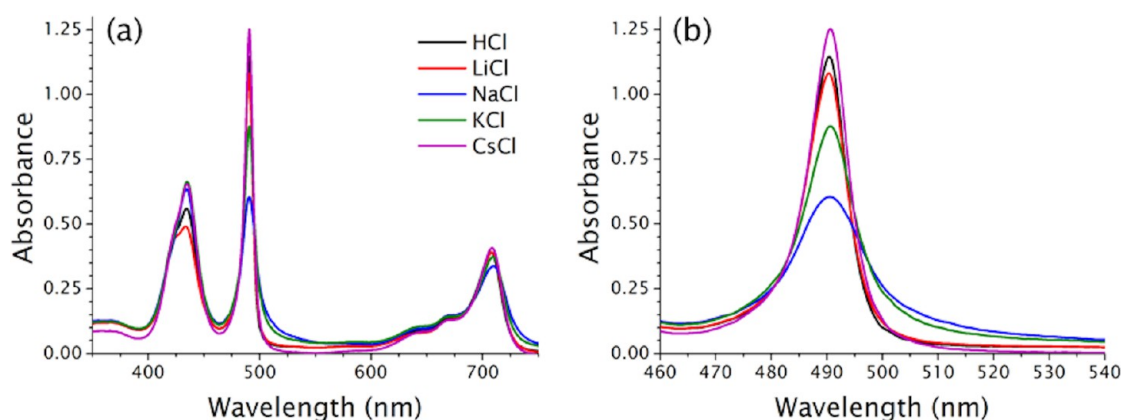
Figure 3. Corrected absorbance spectra over full measured range (a) and J band region (b). Solutions are 5 μM TSPP in 0.75 M HCl (black), LiCl (red), NaCl (blue), KCl (green), and CsCl (purple).

(Ted Pella; diluted to 4×10^{-3} % w/v suspension) as a scattering standard.

We refer to the raw data from the spectrophotometer as "extinction" because it includes a non-negligible scattering component in addition to actual absorption. Several studies describe methods for mutually correcting measured extinction and scattering data to yield "true" absorption and RLS spectra.[30,50,51] Ideally, these methods should include particle size and form-factor parameters of the actual samples determined by such methods as dynamic and angular light scattering.[50] However, at low enough optical densities, it is sufficient to correct the instrumental data by fitting raw data for nonabsorbing scatterer and nonscattering absorber standards to that for a mixture containing both scatterer and absorber. The wavelength-indexed data were fit to the model:

$$-\log\left(\frac{I}{S}\right) = qA$$

$$1 - 10^{(A-E)} = pS \qquad (1)$$

where A is the absorbance of the absorption standard, E is the extinction of the mixture, S is the scattering standard intensity, and I is the scattering intensity of the mixture. The fit parameters correspond roughly to an effective path length in the fluorimeter (q) and an effective scattering volume in the spectrophotometer (p). Unspecified characteristics of instrument sources, optics, and detectors also factor into these parameters. The linear regression derivations of these parameters are shown in Figure S1. Regions of poor calibration of the fluorimeter detector response (mainly in the lower sensitivity region of the PMT beyond about 700 nm) were omitted from the determination of the p parameter. Direct comparison of the Q-band region to the Soret region within a single spectrum is thus of limited value. Nevertheless, comparison of corresponding wavelength regions between different samples is not affected by this limitation. The parameters thus derived were applied to the self-consistent nonlinear system:

$$E = A - \log(1 - pS)$$

$$I = S*10^{(-qA)} \qquad (2)$$

Note that these equations are the same as those used by Koti et al.,[30] who implied that their procedure was capable of determining the p and q factors from the sample spectra alone. We were not able to deduce how this was possible without additional equations or a well-defined line shape model. For this reason, we relied on empirically determined values of these parameters.

For each sample, an FFT smoothing algorithm was applied to scattering data to subdue the noise due to stirring. The measured extinction and smoothed scattering spectra were input along with the p and q parameters to a MATLAB function (see Supporting Information), which calculates the absorption and RLS spectra by point-by-point solution to the nonlinear system. A second MATLAB function was used to scale the spectra for differences in the proportion of aggregated porphyrin between samples, so that the aggregate spectral bands as shown in Figures 3 and 5 can be taken to represent approximately 5 μM aggregated porphyrin for all samples.

Additional extinction spectra were acquired for the bottom ~1.5 mL portions of samples prepared as for the other experiments, after standing for 3 days and without agitating, to estimate the degree of sedimentation.

TEM and AFM Imaging. Samples for TEM were prepared by one of two methods: in both cases, a 10 μL drop of the 5 μM TSPP solution was placed on a carbon film-coated, 200 mesh copper grid. In the first method, used for samples in aqueous NaCl and KCl, the drop of solution was allowed to dry completely on the grid. In the second method, used for samples in aqueous LiCl and CsCl, a drop was allowed to stand on the grid for about 5 min before gently wicking off excess solution with filter paper. In either case, the sample was left in a vacuum desiccator overnight to minimize residual water. Micrographs were acquired on a Phillips CM-200 high-resolution TEM with an accelerating voltage of 200 keV.

Samples for AFM were prepared by depositing a small drop (~30 μL) of each sample solution, prepared in the same manner as for the spectroscopic experiments, on a clean mica disc. Tapping mode AFM imaging was performed with the tip driven at resonant frequency 338 kHz on a Veeco Dimension Icon AFM at the Environmental Molecular Sciences Laboratory of Pacific Northwest National Laboratory (EMSL-PNNL).

Optical Imaging. A ~20 μL drop of each solution, prepared as for the other experiments, was placed on a borosilicate glass coverslip. The sample was dried by one of three methods: standing for ~2 h at room temperature, oven drying for ~30 min at ~150 °C, or spin drying for 1 min after standing for 5 min. Images were acquired with an Andor CCD

Table 1. J Band Spectral and Spectrally Derived Coherence Parameters

	integrated extinction/au	absorption fwhm/cm^{-1}	$N_c^{(Abs)}$	$\tilde{C}_{rel}^{(Abs)}$	integrated RLS intensity/au	$\tilde{C}_{rel}^{(RLS)}$
monomer	2255	849	1			
HCl	636	362	5.5	1	537	1
LiCl	635	383	4.9	0.89	582	1.04
NaCl	693	693	1.5	0.27	611	1.07
KCl	711	490	3.0	0.55	373	0.83
CsCl	640	357	5.7	1.04	478	0.94

camera on an Olympus inverted confocal microscope through a 100× oil immersion objective.

RESULTS

Correction of Absorption and RLS Spectra: Application to HCl-Induced Aggregates. A thorough analysis of the relationship between nanostructure and excitonic properties of dye aggregates requires a combination of several complementary spectroscopic and imaging methods. Absorption spectra can be used to screen for aggregation, but interpretation is hazardous without correcting for scattering. The gross structure of these spectra, characterized by a blue-shifted H band and a red-shifted J band, as well as a red-shifted and enhanced Q-band, is remarkably consistent across a wide range of chemical environments and apparent morphologies. The differences between different sample conditions are found mainly in line shapes and fine differences in band locations.

It is often overlooked that spectrophotometric measurements do not necessarily yield a true absorption spectrum. Light scattering may contribute a significant fraction of the total extinction. At the same time, RLS yields information on excitonic coherence, which can be difficult to reliably ascertain from absorption spectra. Unfortunately, typical optical path lengths and the dye concentrations required for appreciable aggregation result in large self-absorption, which distorts the true RLS spectrum. The correction method described in the Experimental Methods is exemplified in raw and corrected extinction and scattering data, shown in Figure 2a and c, respectively, for aggregates in a solution of 5 μM TSPP in 0.75 M aqueous HCl. Similar conditions have been treated in a large body of literature cited in the introduction; thus this sample is our reference for discussion of RLS and coherence (an absolute RLS standard has yet to be developed).

A troubling feature of uncorrected "absorption" spectra of TSPP aggregates in the past has been the much larger integrated absorbance in the J band than in the H band. As seen in Figure 2c, the H band appears much weaker than the J band in total extinction. It is unlikely that aggregation changes the relative transition dipole moments of the two Soret band components of the diacid monomer significantly enough to account for a difference this large. After the scattering contribution has been removed, the integrated absorbance is more nearly equally distributed (695 arbitrary units for the H band vs 740 for the J band). This calculation is a rough estimate but shows that the bulk of the discrepancy of oscillator strength comes from the larger contribution of scattering to the total extinction in the J band than in the H band. The remainder could be related to redistribution of oscillator strength due to asymmetric distortion of the monomers upon aggregation, to larger intensity borrowing by a Q-band component from the H band than from the J band, or to some combination of these or other factors.

Absorption Spectra of TSPP Aggregates in Alkali Halide Solutions. The pH of solutions was adjusted prior to mixing and then finely adjusted with a small amount of 1 M HCl to the range pH 2.6−2.8. This is at the low end of the range at which TSPP is almost entirely dianionic diacid monomer in the absence of additional solutes. Thus, aggregation can be attributed purely to the effect of the salt species. The same procedure for data collection and correction was used as illustrated for aggregates in 0.75 M HCl. An additional correction procedure using reference spectra of pure aggregate (obtained from higher concentration solutions) and pure monomer was performed to estimate the percent composition of aggregated and monomeric porphyrin in the solution. This was then used to scale the spectra so that the J band regions could be compared on an equivalent basis of 5 μM aggregated porphyrin. These scaled spectra over the full visible region are shown in Figure 3a with an expanded view of the J band region in Figure 3b. Integrated extinction values are given in the first column of Table 1. The integral is taken over the entire Soret band for the monomer, from 20 500 cm^{-1} (488 nm) to 26 500 cm^{-1} (377 nm).

The monomer oscillator strength is redistributed to H, J, and Q bands in the aggregate; the values for the aggregates pertain only to the extinction of the J band, integrated from the minimum at 18 000 cm^{-1} (556 nm) to the minimum at 21 500 cm^{-1} (465 nm), to minimize the contribution of other spectral features. The H band is not well resolved from the residual monomer peak, while the Q-band region is spectrally congested with poorly resolved features from both aggregate and residual monomer. Although we recognize the likely significance of coupling between J and Q bands, for these reasons we focus on the J band.

We qualitatively classify the absorption line shapes resulting from the different solution conditions into two primary groups. The first kind displays narrower bands in all regions, especially noticeable in the J band (see Table 1, absorption fwhm). This includes our reference conditions of 0.75 M HCl without additional solutes as well as 0.75 M LiCl and CsCl. In contrast, 0.75 M NaCl leads to distinctly broadened absorption bands. 0.75 M KCl results in line shapes intermediate between these two cases, but as discussed below in consideration of imaging experiments, there are reasons to classify the aggregation behavior of TSPP in KCl as most similar to that in NaCl, albeit with some important differences.

The apparent degree of aggregation decreases with increasing cation size, as evidenced by a correspondingly larger residual monomer peak in the raw extinction spectra (Figure S2). Note that the data scaling applied to make the spectra in Figures 3 and 5 representative of the same amount of aggregated porphyrin obscures this fact. From the similarity of band maxima locations, we infer that similar excitonic coupling strengths generate the major spectral shifts. These are strongly constrained by the local packing geometry,[16] which in this case

is determined primarily by electrostatic interactions between sulfonate groups and protonated porphyrin cores, with some assistance from $\pi-\pi$ van der Waals interactions. We expect this level of structure to be least affected by solution composition and structure. Whether other aspects of the geometry differ, such as tube diameter or length (or even the formation of tubes rather than sheets), cannot be ascertained from this limited information. The details of line shapes, on the other hand, are affected by counterion influences on overall aggregate morphology.

Narrowing of the J band as compared to the monomer Soret band is commonly observed in absorption spectra of excitonically coupled aggregates. Theoretically, this "exchange narrowing" has been variously attributed to a decrease in displacement of the nuclear potential due to sharing of electronic excitation (thus attenuating the Franck–Condon progression and collapsing intensity toward the 0–0 vibronic transition), or to a delocalized excitation averaging over various sources of disorder in the ensemble of coherently coupled monomers.[52,53] Regardless of the microscopic mechanism, it is calculated that the line width should narrow as $N_c^{-1/2}$, disregarding inhomogeneity between distinct aggregates. Here, N_c is the coherence number, the average number of chromophore units over which the excitonic transition is delocalized. For HCl-induced aggregates, this number has been variously estimated at 5–13 from absorption spectrum exchange narrowing,[30,54] and 60–80 from electro-optical effect enhancement.[55]

Referring again to Table 1, N_c calculated directly from the absorption fwhm for each sample is given, denoted $N_c^{(Abs)}$. On the basis of this parameter alone, we would assign an average coherence number of no more than 5.7 and as little as 1.5, depending on the solution conditions. This seems too low on an intuitive level, and in fact has already been contradicted by much evidence, most notably by RLS spectra. Also included in Table 1 is $\tilde{C}_{rel}^{(Abs)}$, the ratio of $N_c^{(Abs)}$ for each sample to that of the reference sample in 0.75 M HCl. Under the naïve assumption of $N_c^{-1/2}$ dependence of absorption bandwidth, we expect N_c to be slightly larger for CsCl-induced as compared to HCl-induced aggregates, and much smaller for NaCl-induced aggregates. The remaining two cases lie between these extremes. $\tilde{C}_{rel}^{(Abs)}$ will be useful for comparison to the RLS results below.

Less spectral narrowing is observed in the H band than in the J band. One explanation is that the H excitons are simply less coherent, so the unresolved vibronic progression is less exchange-narrowed.[25] We need to minimize the amount of residual monomer to get a clearer view of the H band. Extinction spectra for the same salt concentrations but with 50 μM rather than 5 μM TSPP are shown in Figure 4. Here, the aggregation process has gone nearly to completion. Most importantly, the correlations of peak positions and band widths with cation species are the same at both TSPP concentrations. The red shoulder on the H band indicates a very small amount of residual monomer. Allowing for that, the H band still appears broader than the J band in all conditions, consistent with a tendency to lower coherence regardless of solution conditions. Yet it is in the RLS spectra, to which we now turn, where this difference in coherence between the bands becomes most striking.

Resonance Light Scattering Spectra and Variability of Spatial Excitonic Coherence.
RLS spectra for the sample series, corrected for self-absorption and scaled to represent 5 μM aggregated porphyrin, are shown in Figure 5. In most of the
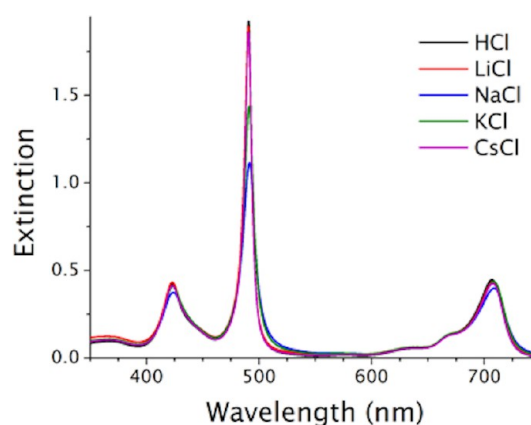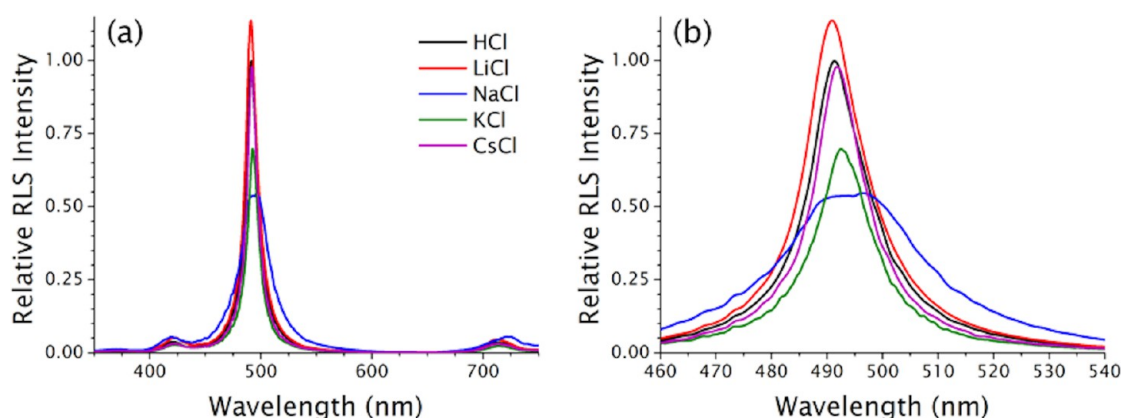

Figure 4. Extinction spectra of TSPP aggregates from 50 μM TSPP in the same series of aqueous solutions as in Figures 2 and 3. Absorbance cell path length = 1 mm.

samples, RLS contributes to the total extinction more toward the red side of the J band (aggregates in HCl, Figure 2b; other samples, Figure S3). This indicates greater coherence of excitonic transitions excited in this region. Correspondingly, the H band has much smaller RLS intensity than the J band, indicative of lower excitonic coherence. These general observations hold well for aggregates prepared in HCl, LiCl, and CsCl, while those prepared in NaCl and to a lesser degree KCl differ notably in having a broader and more symmetric RLS profile in the J band region. It has been shown[56] that for a one-dimensional excitonically coupled aggregate with $N_c \gtrsim 20$, the RLS intensity scales as N_c^2. Thus, we can designate a coherence parameter $\tilde{C}^{(RLS)} \propto (I_{RLS})^{1/2}$, and a relative coherence parameter $\tilde{C}_{rel}^{(RLS)} = \tilde{C}^{(RLS)}(sample)/\tilde{C}^{(RLS)}(reference)$ given a reference sample (here aggregates in 0.75 M HCl). Values of I_{RLS} for the J band, integrated from 17 000 cm^{-1} (588 nm) to 23 000 cm^{-1} (435 nm), and $\tilde{C}_{rel}^{(RLS)}$ for the series of samples are listed in the last two columns of Table 1. Under this simplified treatment of the relation between RLS intensity and excitonic coherence, we thus observe greater coherence for LiCl- and NaCl-induced aggregates, and slightly lower coherence for CsCl-induced aggregates. The coherence parameter is even more notably reduced in KCl solutions. If the J band consisted of a single transition, we would expect close correlation between these two parameters. However, when they disagree, this suggests the absorption line shape arises from multiple transitions, each potentially having its own line width. The discrepancies between $\tilde{C}_{rel}^{(RLS)}$ and $\tilde{C}_{rel}^{(Abs)}$ are thus consistent with composite J-band structure that differs between solution conditions, and the RLS-based measure should be preferred. We propose that larger-scale morphological features described in the next section may increase coherence in the sense of either promoting greater delocalization of excitons or permitting transitions to a greater number of excitonic states. On the other hand, some morphological features may decrease coherence by introducing disorder. These effects further confound the relationship between overall coherence and absorption bandwidth.

Cation-Dependent Morphological Effects Observed by TEM and AFM.
We imaged aggregates deposited from the solutions by TEM (Figures 6 and 10) and AFM (Figures 7–9, 11) to identify morphological features that may correlate with the spectroscopic observations. The following comments deal with these images according to sample.

Figure 5. Corrected RLS intensity (relative to peak intensity in HCl solution) spectra over full measured range (a) and J band region (b) for the same series of solutions as in Figure 2.
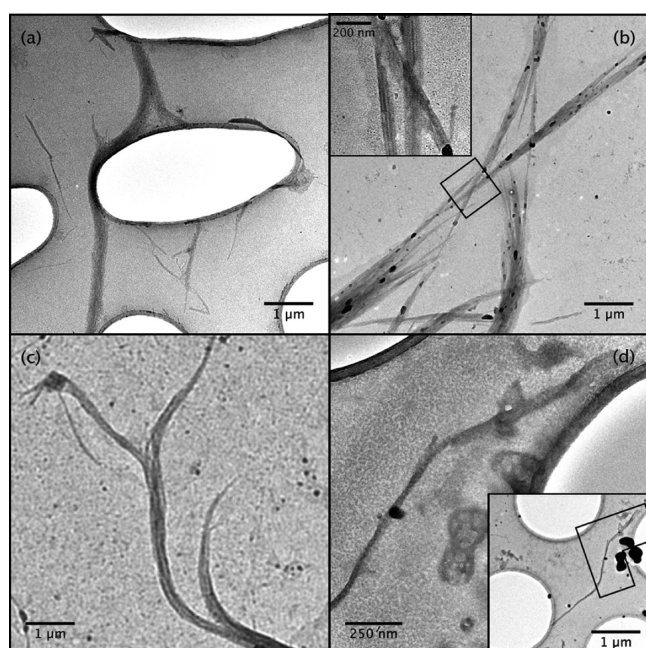
Figure 6. TEM micrographs of TSPP aggregates deposited from 5 μM TSPP in 0.75 M alkali chlorides: (a) LiCl, (b) NaCl, (c) KCl, and (d) CsCl. Note that the inset of (d) is at the scale of images (a), (b), and (c), while the larger field shows higher resolution detail of the indicated area.

Figure 6a is a TEM image of aggregates deposited from LiCl solution. Elongated structures ranging from about 100 nm to over 10 μm are observed. Widths range from about 10 to 500 nm. There is no obvious indication of hierarchical structure, other than the tendency of wider structures to be darker, suggestive of thicker layers of material. No nanotubular subunits are observed, so any such structure is likely due to multiple layers of open sheets, or possibly nested tubes.

An AFM image of lithium chloride-induced aggregates in Figure 7a shows variable aggregate dimensions, both within a single structure and between different structures. Height profiles (Figure 7b) are shown for three locations in the image. One narrower section (labeled (1) on the image) is 184 nm in width. The wider section (2) is 408 nm across and 19 nm in height, while another narrow section (3) is 203 nm in width and 11 nm in height. No evidence of composite structure, such as steps or grooves, is observed in these profiles.

Because of the deliquescence of LiCl, there may be a significant water layer on the surface of these aggregates, which could obscure such features. However, no evidence of water was observed in the corresponding TEM images, where special care was taken to minimize exposure to the atmosphere. This contrasts with the case of NaCl, where small, dark regions within aggregate bundles visibly produced vapor when observed under the focused electron beam, evidence that they contained water. Thus, it is unlikely that there is hidden nanotubular structure in LiCl-induced aggregates. Multilayered or nested morphology seems more likely when the TEM and AFM results are considered together.

In contrast, aggregates deposited from aqueous NaCl exhibit an architecture of orderly bundles of nanotubes. The TEM image in Figure 6b displays bundles of comparatively rigid individual strands, anywhere from 3 or 4 to perhaps 50 or more strands per bundle. In a close-up image of a narrow section of the bundle (Figure 6b, inset), the individual strands are relatively straight and have long sections of parallel orientation. These strands, seen more clearly in the higher magnification inset, are about 20−25 nm in width, consistent with flattened nanotubular structures of size similar to those found in images of HCl-induced TSPP aggregates (see Figure S4).

AFM data in Figure 8 corroborate these observations. The individual elongated features visible within the bundles are typically about 25 nm in diameter. Steps and grooves are observed in the height profiles, with heights of bundles and the numbers of step features consistent with 3−4 nm height per layer of subunits (particularly in the smaller section in height profile 2 of Figure 8b). This again comports with observations of collapsed nanotubular structures in the case of HCl-induced aggregates.[11,15] The structures do not exhibit any regular packing geometry, a salient feature for interpretation of morphological−optical property relationships treated in the discussion.

In the TEM image of aggregates deposited from aqueous KCl (Figure 6c), bundled structures are also observed, but here are composed of a smaller number of strands. These appear to bend smoothly, as if more flexible. In another image (Figure S5a), a higher magnification TEM image of a smaller bundle resolves individual tubes, showing how component nanotubes appear to bend and twist around each other.
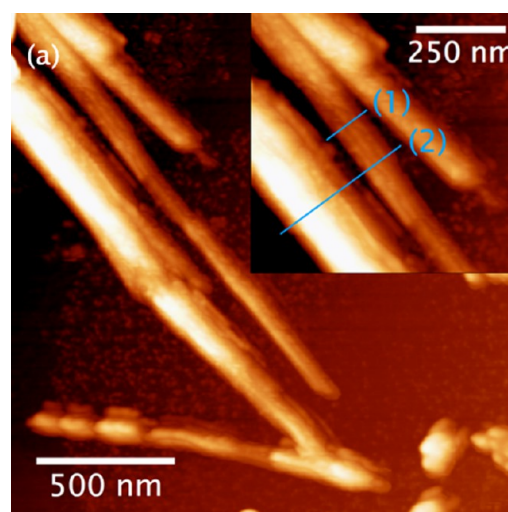
The AFM image of KCl-induced aggregates (Figure 9) shows evidence of bundled morphology, with height profiles indicating a small bundle having subunits ∼30 nm in width
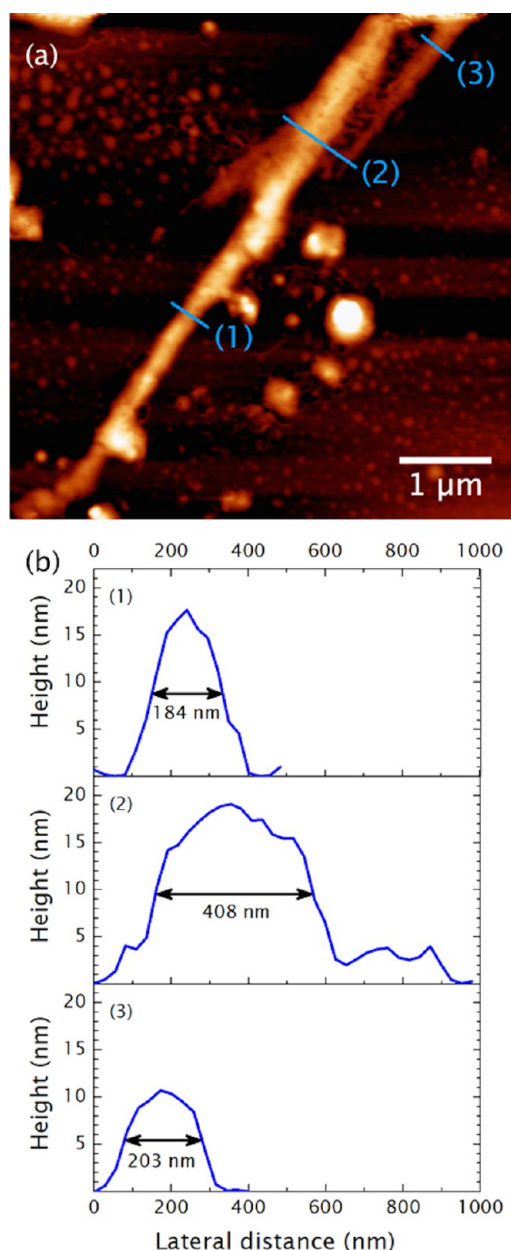
Figure 7. (a) AFM images of aggregates deposited from 5 μM TSPP in 0.75 M LiCl. (b) Cross-sectional height profiles at the locations labeled in (a).

Figure 8. (a) AFM images of aggregates deposited from 5 μM TSPP in 0.75 M NaCl. (b) Cross-sectional height profiles at locations labeled in (a).

and ~4 nm in height. Another AFM image is provided in Figure S6. This image, however, lacks clear indication of a regular subunit size. While we cannot rule out the possibility of tubes of larger and variable diameter forming in KCl, given evidence from TEM of large quantities of salt solidifying on the aggregates (Figure S5b), we propose that these larger and variable widths are mainly due to a coating of salt. Overall, more structural inhomogeneity is observed in the presence of KCl than the other salts.

A TEM image of the final aggregate sample, deposited from CsCl solution, is shown in Figure 6d. This structure is several micrometers in length, with perhaps two or three tubes at most in wider sections. The narrower and wider sections could represent intact and collapsed regions of nanotubes, and are perhaps slightly wider than those observed in the HCl-induced case.

Figure 10 shows a TEM image of an individual nanotube deposited from the same CsCl solution, the helical lattice structure of which can be seen clearly in the first detail image. The tube diameter (~16 nm), separation of adjacent helices (~1 nm), as well as the helical pitch (~25°) are consistent with those reported in the literature for HCl-induced aggregates.[17,27] A second detail image shows a square lattice structure with spacing of about 4.1 Å, consistent with the lattice constant of CsCl. Thus, the slightly larger apparent widths are likely due to a coating of CsCl deposited on the nanotubes. The cloudy regions extending about 2−3 nm beyond the darker edges of the inner nanotube structure are likely due to a disordered salt layer.

An AFM image of aggregates deposited from CsCl solution (Figure 11a) shows individual nanotubes as well some small bundles of 2−3 tubes. Profiles give heights of about 3.5 nm and widths just over 30 nm for individual tubes. These are again wider than observed for HCl-induced aggregates, consistent with salt deposition on and around the tubes. It is possible that here the salt accumulates mainly to the sides as the solution
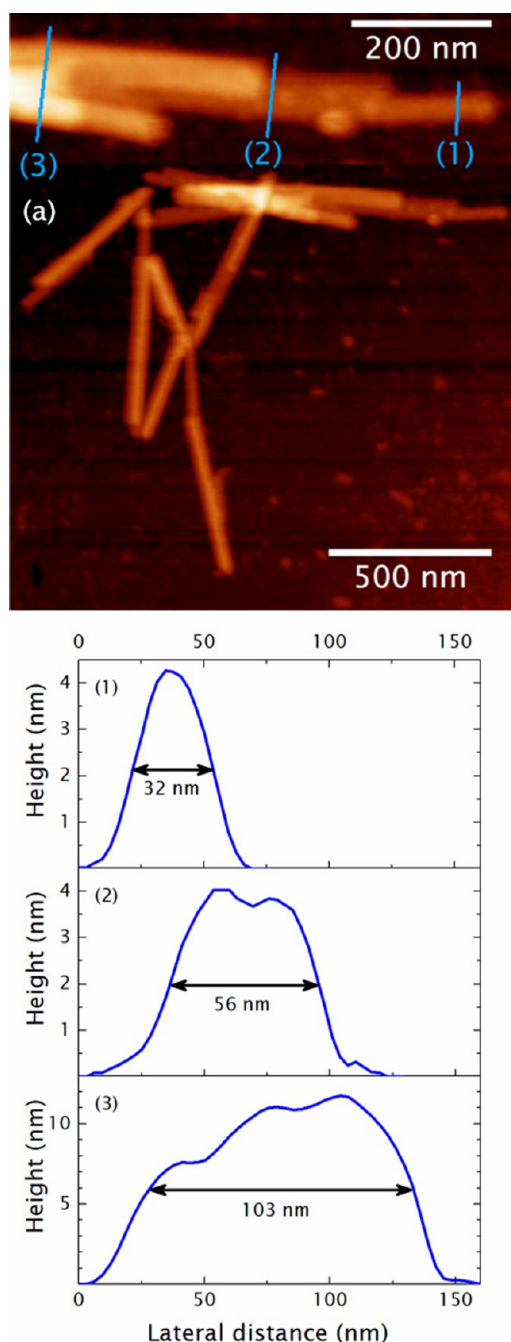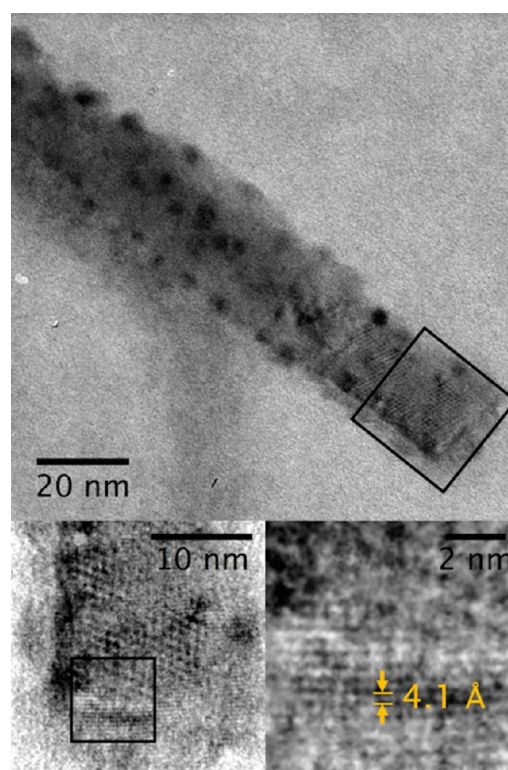
Figure 9. (a) AFM images of aggregates deposited from 5 μM TSPP in 0.75 M KCl. (b) Cross-sectional height profiles at locations labeled in (a).

Figure 10. Top: TEM micrograph of a single nanotubular aggregate deposited from 5 μM TSPP in 0.75 M CsCl. Bottom left: Detail of boxed area in top image, showing diagonal lattice pattern. Bottom right: Detail of boxed area on bottom left, showing square lattice pattern with spacing consistent with CsCl lattice constant.

dries, adding perhaps ∼2−3 nm on each side (∼4−6 nm total) to the overall width, while not increasing the height by more than a fraction of a nanometer.

Optical images in Figure S7 indicate that large-scale morphology does not depend on deposition method. Along with the TEM and AFM images presented above, these show consistency among different substrates (carbon film, mica, or borosilicate glass), deposition times (5 min to 2 h), and drying methods (air drying at room temperature or ∼150 °C, spin drying, or blotting followed by vacuum drying). Extinction spectra of flocculated aggregates agree in line shape with those of the corresponding well-mixed solutions (Figure 8a). The extinction/concentration ratio of the sediment-containing

portion to the well-mixed solution (inset table of Figure S8b) is related to aggregate density and characteristic cross-sectional area. KCl- and NaCl-induced aggregates have comparatively larger values of this ratio, consistent with the formation of dense structures, as through bundling. The intermediate value for CsCl-induced aggregates may result from longer tubes and a small amount of bundling, while LiCl-induced aggregates may give a small value due to lower density relative to size.
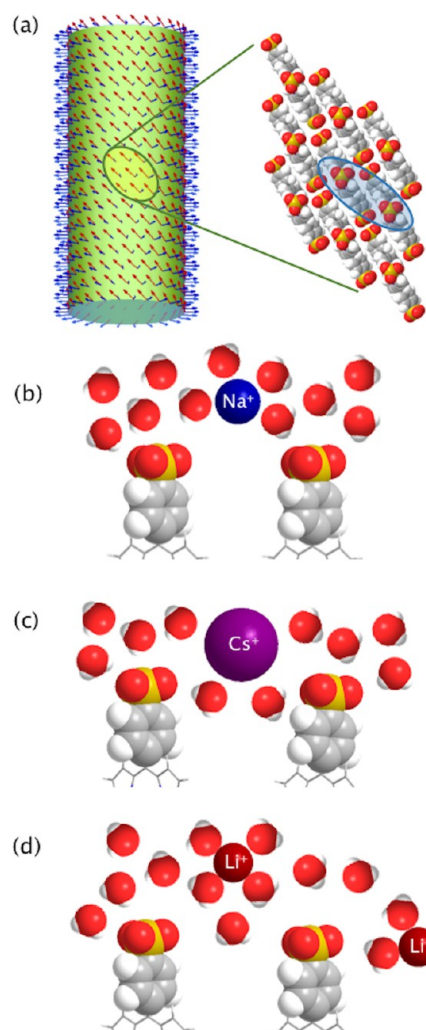
■ DISCUSSION

Having separately detailed spectroscopic and imaging results for each of the four salt-induced aggregate samples, and compared these results to the reference case of HCl-induced aggregates, we can discuss some relationships between the morphological features and spectroscopic properties.

Widths and thicknesses of nanotubular components are similar among aggregates induced by three of the salts: NaCl, KCl, and CsCl. Apparently wider and thicker aggregates in the presence of the latter two salts may be due to a larger amount of salt deposited on them. Because of strong similarities between the lattice structure observed for a nanotube deposited from CsCl (Figure 10) and the structure of HCl-induced aggregates described in refs 13 and 23, it is reasonable to expect a similar, although not necessarily identical, multihelical structure of nanotubular units induced by NaCl, KCl, and CsCl. In the absence of high-resolution images of the molecular lattice in the case of NaCl- and KCl-induced aggregates, other models that account for the crucial properties cannot be ruled out. However, a preponderance of theoretical and experimental evidence suggests that porphyrin−porphyrin interactions are
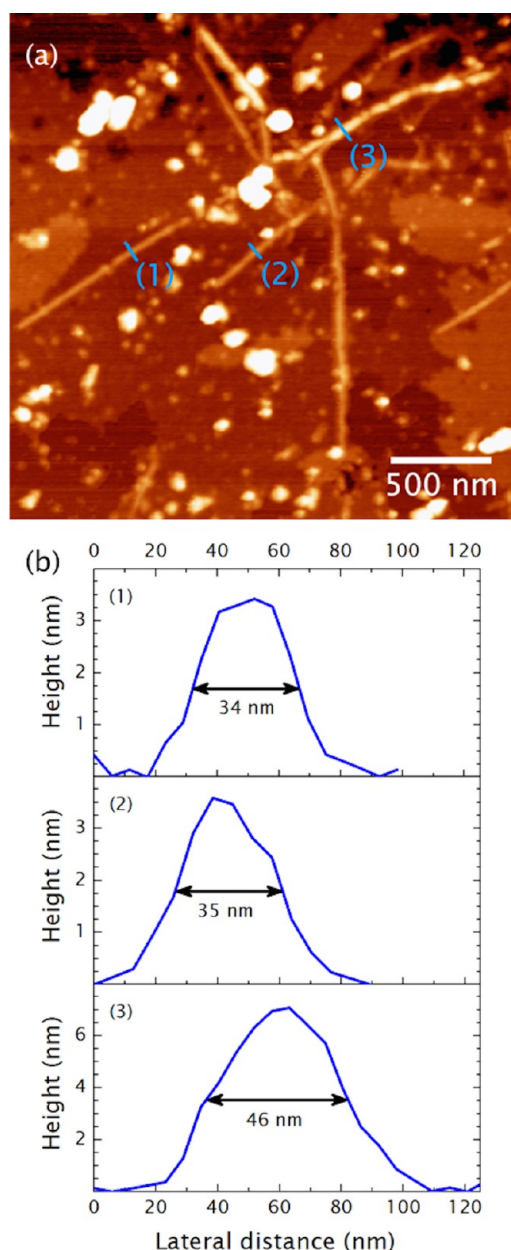
Figure 11. (a) AFM images of aggregates deposited from 5 μM TSPP in 0.75 M CsCl. (b) Cross-sectional height profiles at locations labeled in (a).

Figure 12. (a) Local lattice structure related to helical nanotube with transition dipole moments as first depicted in Figure 1. (b)−(d) Illustrative cartoons of local solvation environment near pairs of radially oriented sulfonatophenyl groups in the presence of (b) Na$^+$, (c) Cs$^+$ (K$^+$ is expected to be similar), and (d) Li$^+$.

the dominant factor determining internal structure (depicted in Figure 12a) and that this structure does not vary significantly among these solution conditions. Modeling has shown that the splitting between J and H bands (nearly identical in the experimental spectra of these samples) is highly sensitive to internal orientation angles.[16] These angles are constrained by diameter and wall thickness. Diameters and thicknesses derived from small-angle X-ray scattering for aggregates formed in the presence of buffer solution with a mixture of Na$^+$ and K$^+$ are the same as those derived from imaging and diffraction studies of HCl-induced aggregates.[57] Finally, no frequency shifts are observed in solution phase resonance Raman spectra (to be presented in a forthcoming publication), regardless of the salt used. We would expect some mode frequencies to vary if there were major differences in the lattice structure or tight association of counterions with the porphyrin molecules.

Regardless of these considerations, only the directions and rough relative magnitudes of transition dipole components contributing to the H- and J-band matter for the rest of this discussion, so the detailed molecular lattice structure is hereafter ignored. We need only consider two key morphological features to explain the differences in the J-band shapes and relative RLS intensities: bundling of multiple nanotubes and softening of individual tubes (observed as bending in the images).

Some theoretical considerations regarding helical excitons are needed for our discussion of these morphological effects. Knoester and co-workers have dealt with this theory in detail, from which we draw a few key points.[16,28,58,59] A helical nanotube can be constructed as a stack of N_1 rings, each having N_2 monomers (which is also the number of helices composing the nanotube). Each monomer can be assigned an index vector $\mathbf{n} = (n_1, n_2)$, where n_1 is the index of the ring and n_2 is the index of the helix along which the monomer is located, running in integer steps from 1 to N_1 or N_2, respectively. A helix is defined as the path between monomers at angle of rotation γ on successive rings.

We consider only the doubly degenerate Soret band of the monomers, consisting of a pair of orthogonally polarized transitions $p = x, y$. The complete set of possible one-molecule excited states, designated $|np\rangle$, forms a complete basis in real space. In a disorder-free aggregate of length much greater than diameter, full cylindrical symmetry permits periodic boundary conditions to be applied both around the rings and along the helices. This idealization allows us to make a unitary transformation from real to reciprocal space. In this representation, the basis functions, indexed by the excitonic wavevector $\mathbf{k}$, are

$$|\mathbf{k}p\rangle = \frac{1}{\sqrt{N}} \sum_{\mathbf{n}} \exp[-i(k_1\varphi_1 n_1 + k_2\varphi_2 n_2)]|np\rangle \tag{3}$$

For each $\mathbf{k}$, there are two eigenstates ($\alpha = 1,2$) of the transformed Hamiltonian, corresponding to the mixing and splitting of the two Soret band components:

$$|\mathbf{k}\alpha\rangle = \frac{1}{\sqrt{N}} \sum_{p} c_p^{(\alpha)}|\mathbf{k}p\rangle \tag{4}$$

with total number of monomers $N = N_1 N_2$, excitonic wavevector $\mathbf{k} = (k_1,k_2)$, and phase increment $\varphi_1 = 2\pi/N_i$. Transition dipole matrix elements between the ground state and these excitonic states vanish for all values of k_2 except 0, 1, and −1. Transition to the $k_2 = 0$ exciton is allowed for light polarized in the axial direction. Transitions to the doubly degenerate pair of excitons $k_2 = \pm 1$ are allowed for light polarized perpendicularly to the tube axis. It has been shown that in the limit of large N_1, $k_1 = 0$ when $k_2 = 0$ and $k_1 = \pm\gamma/\varphi_1$ when $k_2 = \pm 1$. The $\mathbf{k} = 0$ exciton has all monomer wave functions in phase, while the $\mathbf{k} = \pm(\gamma/\varphi_1, 1)$ excitons have a nodal plane containing the long axis and dividing the tube into two halves of opposite phase. For smaller aggregates in which periodic boundary conditions do not apply in the direction of the tube axis, k_1 is not a good quantum number, and states of more complex geometry become allowed. Symmetry lowering, as from bundling, and disorder related to loosening of intermonomer forces or defects, can similarly relax the restrictions of this model and allow a greater number of excitonic transitions.[59]

Bundling is observed most prominently in NaCl-induced aggregates, which show the broadest J band in the absorption spectrum and the greatest integrated RLS intensity. Crucially, large regions of multiple, well-aligned nanotubes are prevalent in these conditions. An interesting similarity has been seen in carbocyanine C8S3 nanotubes, which have a split J band, the components of which broaden and increase in separation when the tubes form bundles.[60] Let us assume that prior to bundling, there are distinct J band components polarized in the direction of the tube axis and tangentially to the circumference of the tube as deduced previously for HCl-induced aggregates. For the tangentially polarized J band component, only the doubly degenerate pair of excitons, each with two nodes, is active. When bundles form, symmetry lowering can activate states of higher excitonic wavenumber k_2. Analogously, imperfect alignment of tubes is a disordering influence that could redistribute intensity from $k_1 = 0$ to higher k_1 excitons. These effects distribute the oscillator strength more broadly across the tangentially and axially polarized excitonic manifolds, contributing to the observed broadening.

The explanation for increased RLS intensity in this case is fairly straightforward. For two overlapping excitonic transitions of the same optical polarization to states A and B, RLS intensity scales with coherence number no more rapidly than $(N_{C,A} + N_{C,B})^2$, where $N_{C,A}$ and $N_{C,B}$ are the coherence numbers associated with the two states (details are given in the Supporting Information). This readily generalizes to larger numbers of excitons with overlapping absorption profiles. Thus, we can say that a greater relative RLS intensity indicates a greater overall excitonic coherence in one or both of two ways: larger coherence numbers associated with a fixed set of excitonic states, and/or a greater number of allowed excitonic transitions. Additionally, axially polarized excitons could decrease in coherence at the same time as tangentially polarized excitons increase in coherence, as long as the latter increase is large enough. This would contribute additional broadening through decreased exchange narrowing of the axially polarized J-band component, consistent with the broader absorption line shape and greater integrated RLS intensity of the J band for NaCl-induced aggregates.

In contrast to these effects of bundling, softening of nanotube lattices and highly disordered bundling and intertwining would tend to limit the extent of aligned regions of nanotubes and thus decrease coherence. Spano provides a statistical treatment of the effects of disorder on excitonic coherence.[61] Central to this treatment is the definition of the coherence number:

$$N_C \equiv \frac{1}{\langle C^{(\mathbf{k}\alpha)}(0)\rangle} \sum_{s=-(N-1)}^{N-1} |\langle C^{(\mathbf{k}\alpha)}(s)\rangle| \tag{5}$$

$C^{(\mathbf{k}\alpha)}$ is the coherence function, defined in terms of the excitonic states discussed above as

$$C^{(\mathbf{k}\alpha)}(s) \equiv \sum_{n} \langle \mathbf{k}\alpha|B_n^\dagger B_{n+s}|\mathbf{k}\alpha\rangle \tag{6}$$

The angle brackets in the expression for N_C indicate an average over a statistical ensemble of configurations of disorder. This ensemble characterizes the inhomogeneity between distinct aggregates in a sample. For each such configuration, the coherence function provides a profile of correlated excitation of monomers contributing to the overall excitonic wave function versus the number of sites s separating a given pair of monomers. In the absence of disorder and with periodic boundary conditions, monomer excitations within each configuration are perfectly correlated, leading to $N_C = N$, the total number of monomers in the aggregate. In the opposite, maximally disordered limit, monomer excitations are completely uncorrelated, and $N_C = 1$. Realistic cases involving correlated disorder lie somewhere between these two extremes. Vacancies, dislocation defects, lattice distortions, and orientational disorder associated with softening introduce spatially correlated disorder via disruptions to the regular lattice geometry. Consequently, irregularity is introduced into the intermonomer coupling strengths, decreasing the value of the coherence function in each configuration. This corresponds to a limitation on excitonic delocalization and a smaller average N_C for the sample.

CsCl-induced aggregates appear to be the most flexible, as well as exhibiting the least amount of bundling. There is a small decrease in the coherence relative to HCl-induced aggregates in this case that can likely be attributed to softening giving rise to small-scale orientational disorder. The appearance of some intertwined pairs and triples in the images also suggests the possibility that poorly aligned contact regions detract from the

proportion of aggregate area suited to host excitons of large coherence number.

In the case of KCl, a large amount of bundling is observed along with intertwining of component nanotubes. Here, there is a decrease in coherence as measured by RLS intensity, but also a significant broadening in the absorption spectrum. There may be some activation of the tangentially polarized J excitons, but softening and intertwining likely limit the coherence of both J band components to an even greater extent than with CsCl-induced aggregates. There may be additional static disorder due to the presence of salt in the interstices between the nanotubes that similarly limits the coherence. Thus, the significantly smaller RLS intensity as compared to HCl-induced aggregates makes sense in light of these disordering influences of the morphology.

In contrast to aggregates formed in the other solutions, LiCl-induced aggregates likely have a fundamentally different, multilayered or nested architecture, in which the nanotubular subunits observed in the other samples may differ greatly or be absent. Here, the higher RLS intensity could be due to a higher density of monomers in close proximity within a layered structure as compared to nanotubes. The absorption line shape is only slightly broadened in comparison to HCl-induced aggregates, which makes sense if there are selection rules at play different from those invoked to explain the broadening observed in the presence of Na^+ and K^+. These structures also appear somewhat flexible, but perhaps the size in the directions perpendicular to the length is sufficient to outweigh disordering effects of softening along the length.

For the final portion of our discussion, we suggest some mechanisms by which different counterions may induce the observed variations in aggregate morphology. For this, we turn to kosmotropic versus chaotropic designations and the ranking of the alkali cations by the Hofmeister series. In the case of alkali ions, Li^+ and Na^+ are typically classified as strongly and weakly kosmotropic, respectively, while K^+, Rb^+, and Cs^+ are considered progressively more chaotropic. The Hofmeister series follows this same ordering, for the most part, based on the effects of these ions on protein solubility. The following arguments are highly qualitative and subject to a complex set of uncertainties, and so should be considered a first, suggestive attempt to interpret the observations.

The empirical "law of matching water affinities" states that ions closer on the kosmotropic−chaotropic ranking tend to associate more favorably, as their solvation shells are in some sense more compatible. The peripheral sulfonate groups of TSPP are expected to be chaotropic, like methanesulfonate, which preferably pairs with K^+ over Na^+ in simulations.[62] Simulations of sulfobetaine zwitterions (which have a sulfonate group and a cationic tertiary amine group connected by a short hydrocarbon chain) have shown more favorable interaction with chaotropic than kosmotropic ions.[63] Thus, we expect ion-pairing affinities for sulfonate groups to be stronger for K^+ and Cs^+ and weaker for Na^+. Li^+ displays some anomalous behavior due to its extremely strong water affinity, which may lead to some of the unique features of aggregates induced by LiCl.

Because Na^+ has stronger water affinity than sulfonate and is repelled by the π-conjugated portions of the porphyrin molecules (Figure 12b), it should draw water away from the porphyrins, strengthening hydrophobic interactions between monomer units and increasing nanotube rigidity. More labile sulfonate−Na^+ pairing could allow either for Na^+ to coordinate between sulfonate groups on different nanotubes, or for Cl^- to

coordinate between Na^+ ions at these surfaces. These effects could explain the prevalence of bundling in NaCl-induced aggregate samples.

The weak water affinity of Cs^+ may favor closer association with sulfonate groups (Figure 12c) and greater disorder in the nanotube solvation environment compared to pure water. This would weaken the hydrophobic interactions between porphyrin monomers, resulting in the presumed softening observed as nanotube bending. Along with relatively lower affinity between Cl^- and Cs^+, more effective charge neutralization due to closer Cs^+ association at nanotube surfaces would disfavor bundling.

For KCl-induced aggregates, nanotube flexibility could arise from similar chaotrope−chaotrope pairing effects as with CsCl. We also expect K^+ to have the most closely matched water affinity with Cl^- among the several cations studied. A TEM image (Figure S3b) shows evidence of salt crystals deposited on KCl-induced aggregates. This suggests significant association between K^+ and Cl^- on these aggregates, providing nucleation sites for KCl crystallization during sample drying. The higher occurrence of both K^+ and Cl^- inserted between subunits would serve as an additional disordering, coherence-limiting influence. It is possible that both Na^+ and K^+ have sizes more suitable to coordinate between nanotubular subunits than Cs^+.

Li^+ has especially strong water affinity, so most Li^+ ion pairing occurs through indirect water-bridged or shared interactions (Figure 12d). Additionally, water-bridging between cations and benzene increased the solubility of benzene in simulations of aqueous solutions containing Li^+ as compared to those containing other alkali ions besides Cs^+, in line with experimental observations.[64] We should therefore consider both the high affinity of Li^+ for water and its potential to insert into the solvation shell of the π-conjugated system. The net effect would be increased aggregate hydration and less favorable conditions to form closed tubes of regular diameter.

■ CONCLUSIONS

By comparing absorption and resonance light scattering spectra along with TEM and AFM images of TSPP aggregates induced by different alkali chlorides, we have correlated counterion-dependent morphological features with optical properties related to excitonic band structure and spatial coherence. For aggregates induced by either NaCl or KCl, a large amount of bundling is observed, which could both inhomogeneously broaden absorption spectra and activate a broader subset of excitonic transitions within the J-band. With NaCl, the existence of large bundles with well-aligned regions of nanotubular subunits leads to an increase in spatial coherence and RLS intensity, likely through excitonic coupling of monomer units over multiple nanotubes. By contrast, the bundling of aggregates in the presence of KCl is much more disorderly, with salt deposits likely included in the bundles and nanotubes tending to twist around each other. This introduces disorder and leads to lower coherence as measured by RLS. The lower degree of bundling in the presence of CsCl and the apparent lack of hierarchical structure in the presence of LiCl result in absorption spectra that are narrower as compared to aggregates induced by the other two salts. With CsCl, flexibility of nanotubes could explain the observed slight decrease in RLS intensity. For aggregates induced by LiCl, it is possible that the observed boost in coherence results from more densely packed monomers in cross-section as compared to aggregates in other solution conditions.

We have also made some tentative suggestions as to the mechanisms by which the different counterions lead to the observed differences in aggregate morphology. The kosmotropic effects of Na^+ can account for the observed rigidity of individual nanotubes. The marginally chaotropic effects of K^+ lead to increased nanotube flexibility, and the high affinity between K^+ and Cl^- allows significant quantities of KCl to solidify in the bulk and on the surface of aggregate bundles. In both cases, bundling may either be due to these ions being within an optimal size range to intercalate between sulfonates of neighboring nanotubes, or be due to having labile coordination with the sulfonates that permits the coordination of alkali ions with Cl^-, allowing the salt to act as "mortar" between nanotube "bricks". By contrast, CsCl-induced aggregates may exhibit less bundling due to either Cs^+ being too large to stably bridge neighboring nanotubes, or to Cs^+ binding too tightly to the sulfonates of individual nanotubes to allow for either direct or Cl^--mediated bridging between sulfonates of different nanotubes. The paradoxical effects of Li^+ can be explained by its unusually strong binding of solvation water, leading to water-mediated interactions with the sulfonates (and possibly with the aromatic rings as well), making a closed nanotubular structure less favorable.

Our results demonstrate that simple and inexpensive changes to solution environment can influence excitonic coherence, geometry, and absorption bandwidth, in ways similar to bacteriochlorophyll complexes. We are presently applying resonance Raman spectroscopy to probe excitonic structure in greater depth, as well as additional high-resolution imaging to better characterize internal structures. Extending our approach to other solvents and solution additives will help sharpen these tools to improve light-harvesting properties of supramolecular aggregates.

ASSOCIATED CONTENT

Supporting Information

The Supporting Information is available free of charge on the ACS Publications website at DOI: 10.1021/acs.jpcc.5b08849.

> Derivation of parameters and MATLAB code for extinction and scattering spectral correction, raw extinction spectra of all samples, additional TEM images of HCl- and KCl-induced aggregates, additional AFM data for KCl-induced aggregates, optical images of aggregates, UV−visible spectra of flocculated aggregates, and theoretical considerations for interpretation of RLS spectra (PDF)

AUTHOR INFORMATION

Corresponding Author

*E-mail jmchale@wsu.edu.

Notes

The authors declare no competing financial interest.

ACKNOWLEDGMENTS

REFERENCES

(1) Scholes, G. D.; Fleming, G. R.; Olaya-Castro, A.; van Grondelle, R. Lessons from Nature about Solar Light Harvesting. *Nat. Chem.* **2011**, *3*, 763−774.

(2) Strümpfer, J.; Şener, M.; Schulten, K. How Quantum Coherence Assists Photosynthetic Light-Harvesting. *J. Phys. Chem. Lett.* **2012**, *3*, 536−542.

(3) Ganapathy, S.; Oostergetel, G. T.; Wawrzyniak, P. K.; Reus, M.; Chew, A. G. M.; Buda, F.; Boekema, E. J.; Bryant, D. A.; Holzwarth, A. R.; de Groot, H. J. Alternating Syn-Anti Bacteriochlorophylls Form Concentric Helical Nanotubes in Chlorosomes. *Proc. Natl. Acad. Sci. U. S. A.* **2009**, *106*, 8525−8530.

(4) Oostergetel, G. T.; Amerongen, H.; Boekema, E. J. The Chlorosome: A Prototype for Efficient Light Harvesting in Photosynthesis. *Photosynth. Res.* **2010**, *104*, 245−255.

(5) Wang, J.; Brune, D. C.; Blankenship, R. E. Effects of Oxidants and Reductants on the Efficiency of Excitation Transfer in Green Photosynthetic Bacteria. *Biochim. Biophys. Acta, Bioenerg.* **1990**, *1015*, 457−463.

(6) Saga, Y.; Shibata, Y.; Tamiaki, H. Spectral Properties of Single Light-Harvesting Complexes in Bacterial Photosynthesis. *J. Photochem. Photobiol., C* **2010**, *11*, 15−24.

(7) Berlepsch, H. von; Böttcher, C. Network Superstructure of Pseudoisocyanine J -Aggregates in Aqueous Sodium Chloride Solution Revealed by Cryo-Transmission Electron Microscopy. *J. Phys. Chem. B* **2002**, *106*, 3146−3150.

(8) Berlepsch, H. von; Böttcher, C.; Ouart, A.; Burger, C.; Dähne, S.; Kirstein, S. Supramolecular Structures of J-Aggregates of Carbocyanine Dyes in Solution. *J. Phys. Chem. B* **2000**, *104*, 5255−5262.

(9) Didraga, C.; Pugžlys, A.; Hania, P. R.; Berlepsch, H. von; Duppen, K.; Knoester, J. Structure, Spectroscopy, and Microscopic Model of Tubular Carbocyanine Dye Aggregates. *J. Phys. Chem. B* **2004**, *108*, 14976−14985.

(10) Berlepsch, H. von; Kirstein, S.; Böttcher, C. Supramolecular Structure of J-Aggregates of a Sulfonate Substituted Amphiphilic Carbocyanine Dye in Solution: Methanol-Induced Ribbon-to-Tubule Transformation. *J. Phys. Chem. B* **2004**, *108*, 18725−18733.

(11) Friesen, B. A.; Nishida, K. R. A.; McHale, J. L.; Mazur, U. New Nanoscale Insights into the Internal Structure of Tetrakis(4-Sulfonatophenyl) Porphyrin Nanorods. *J. Phys. Chem. C* **2009**, *113*, 1709−1718.

(12) McHale, J. L. Hierarchal Light-Harvesting Aggregates and Their Potential for Solar Energy Applications. *J. Phys. Chem. Lett.* **2012**, *3*, 587−597.

(13) Schwab, A. D.; Smith, D. E.; Rich, C. S.; Young, E. R.; Smith, W. F.; de Paula, J. C. Porphyrin Nanorods. *J. Phys. Chem. B* **2003**, *107*, 11339−11345.

(14) Rotomskis, R.; Augulis, R.; Snitka, V.; Valiokas, R.; Liedberg, B. Hierarchical Structure of TPPS₄ J-Aggregates on Substrate Revealed by Atomic Force Microscopy. *J. Phys. Chem. B* **2004**, *108*, 2833−2838.

(15) Rich, C. C.; McHale, J. L. Influence of Hydrogen Bonding on Excitonic Coupling and Hierarchal Structure of a Light-Harvesting Porphyrin Aggregate. *Phys. Chem. Chem. Phys.* **2012**, *14*, 2362.

(16) Vlaming, S. M.; Augulis, R.; Stuart, M. C. A.; Knoester, J.; van Loosdrecht, P. H. M. Exciton Spectra and the Microscopic Structure of Self-Assembled Porphyrin Nanotubes. *J. Phys. Chem. B* **2009**, *113*, 2273−2283.

(17) Short, J. M.; Berriman, J. A.; Kübel, C.; El-Hachemi, Z.; Naubron, J.-V.; Balaban, T. S. Electron Cryo-Microscopy of TPPS₄· 2HCl Tubes Reveals a Helical Organisation Explaining the Origin of Their Chirality. *ChemPhysChem* **2013**, *14*, 3209−3214.

(18) Pasternack, R. F. Aggregation Properties of Water-Soluble Porphyrins. *Ann. N. Y. Acad. Sci.* **1973**, *206*, 614−630.

(19) Ribó, J. M.; Crusats, J.; Farrera, J.-A.; Valero, M. L. Aggregation in Water Solutions of Tetrasodium Diprotonated Meso-Tetrakis(4-Sulfonatophenyl) Porphyrin. *J. Chem. Soc., Chem. Commun.* **1994**, *No. 6*, 681−682.

(20) Ohno, O.; Kaizu, Y.; Kobayashi, H. J-Aggregate Formation of a Water-Soluble Porphyrin in Acidic Aqueous Media. *J. Chem. Phys.* **1993**, *99*, 4128.

(21) Kitahama, Y.; Kimura, Y.; Takazawa, K. Study of Internal Structure of *meso*-Tetrakis (4-Sulfonatophenyl) Porphine J-Aggregates in Solution by Fluorescence Microscope Imaging in a Magnetic Field. *Langmuir* **2006**, *22*, 7600−7604.

(22) El-Hachemi, Z.; Escudero, C.; Arteaga, O.; Canillas, A.; Crusats, J.; Mancini, G.; Purrello, R.; Sorrenti, A.; Urso, A. D.; Ribo, J. M. Chiral Sign Selection on the J-Aggregates of Diprotonated Tetrakis-(4-Sulfonatophenyl)porphyrin by Traces of Unidentified Chiral Contaminants Present in the Ultra-Pure Water Used as Solvent. *Chirality* **2009**, *21*, 408−412.

(23) El-Hachemi, Z.; Escudero, C.; Acosta-Reyes, F.; Casas, M. T.; Altoe, V.; Aloni, S.; Oncins, G.; Sorrenti, A.; Crusats, J.; Campos, J. L.; et al. Structure vs. Properties — Chirality, Optics and Shapes — in Amphiphilic Porphyrin J-Aggregates. *J. Mater. Chem. C* **2013**, *1*, 3337.

(24) Akins, D. L.; Zhu, H.-R.; Guo, C. Absorption and Raman Scattering by Aggregated Meso-Tetrakis(p-Sulfonatophenyl) Porphine. *J. Phys. Chem.* **1994**, *98*, 3612−3618.

(25) Friesen, B. A.; Rich, C. C.; Mazur, U.; McHale, J. L. Resonance Raman Spectroscopy of Helical Porphyrin Nanotubes. *J. Phys. Chem. C* **2010**, *114*, 16357−16366.

(26) Rich, C. C.; McHale, J. L. Resonance Raman Spectra of Individual Excitonically Coupled Chromophore Aggregates. *J. Phys. Chem. C* **2013**, *117*, 10856−10865.

(27) Meng, Q.; Zhang, C.; Zhang, Y.; Zhang, Y.; Liao, Y.; Dong, Z. Tunneling Electron Induced Molecular Electroluminescence from Individual Porphyrin J-Aggregates. *Appl. Phys. Lett.* **2015**, *107*, 043103.

(28) Stradomska, A.; Knoester, J. Shape of the Q Band in the Absorption Spectra of Porphyrin Nanotubes: Vibronic Coupling or Exciton Effects? *J. Chem. Phys.* **2010**, *133*, 094701.

(29) Gandini, S. C. M.; Yushmanov, V. E.; Borissevitch, I. E.; Tabak, M. Interaction of the Tetra(4-Sulfonatophenyl)porphyrin with Ionic Surfactants: Aggregation and Location in Micelles. *Langmuir* **1999**, *15*, 6233−6243.

(30) Koti, A. S. R.; Taneja, J.; Periasamy, N. Control of Coherence Length and Aggregate Size in the J-Aggregate of Porphyrin. *Chem. Phys. Lett.* **2003**, *375*, 171−176.

(31) Choi, M. Y.; Pollard, J. A.; Webb, M. A.; McHale, J. L. Counterion-Dependent Excitonic Spectra of Tetra(*p*-Carboxyphenyl)porphyrin Aggregates in Acidic Aqueous Solution. *J. Am. Chem. Soc.* **2003**, *125*, 810−820.

(32) Doan, S. C.; Shanmugham, S.; Aston, D. E.; McHale, J. L. Counterion Dependent Dye Aggregates: Nanorods and Nanorings of Tetra(*p*-Carboxyphenyl)porphyrin. *J. Am. Chem. Soc.* **2005**, *127*, 5885−5892.

(33) Serra, V. V.; Andrade, S. M.; Neves, M. G. P. M. S.; Cavaleiro, J. A. S.; Costa, S. M. B. J-Aggregate Formation in Bis-(4-Carboxyphenyl)porphyrins in Water: pH and Counterion Dependence. *New J. Chem.* **2010**, *34*, 2757.

(34) Wang, J.; Ding, D.; Zeng, L.; Cao, Q.; He, Y.; Zhang, H. Transformation, Memorization and Amplification of Chirality in Cationic Co(iii) Complex−porphyrin Aggregates. *New J. Chem.* **2010**, *34*, 1394.

(35) Castriciano, M. A.; Romeo, A.; Zagami, R.; Micali, N.; Scolaro, L. M. Kinetic Effects of Tartaric Acid on the Growth of Chiral J-Aggregates of tetrakis(4-Sulfonatophenyl)porphyrin. *Chem. Commun.* **2012**, *48*, 4872.

(36) Zhang, L.; Tian, Y.; Liu, M. Ionic Liquid Induced Spontaneous Symmetry Breaking: Emergence of Predominant Handedness during the Self-Assembly of tetrakis(4-Sulfonatophenyl)porphyrin (TPPS) with Achiral Ionic Liquid. *Phys. Chem. Chem. Phys.* **2011**, *13*, 17205.

(37) Zhang, L.; Yuan, J.; Liu, M. Supramolecular Chirality of Achiral TPPS Complexed with Chiral Molecular Films. *J. Phys. Chem. B* **2003**, *107*, 12768−12773.

(38) Ma, H. L.; Jin, W. J.; Xi, L.; Dong, Z. J. Investigation on Solvation and Protonation of Meso-Tetrakis(p-Sulfonatophenyl)-porphyrin in Imidazolium-Based Ionic Liquids by Spectroscopic Methods. *Spectrochim. Acta, Part A* **2009**, *74*, 502−508.

(39) Li, A.; Zhao, L.; Hao, J.; Ma, R.; An, Y.; Shi, L. Aggregation Behavior of the Template-Removed 5,10,15,20-Tetrakis(4-Sulfonatophenyl)porphyrin Chiral Array Directed by Poly(ethylene Glycol)-*block*-Poly(L-Lysine). *Langmuir* **2014**, *30*, 4797−4805.

(40) Gulbinas, V.; Karpicz, R.; Augulis, R.; Rotomskis, R. Exciton Relaxation in Nanotubular TPPS4 Aggregates in Water Solution and in Polymeric Matrix. *Chem. Phys.* **2007**, *332*, 255−261.

(41) De Luca, G.; Romeo, A.; Villari, V.; Micali, N.; Foltran, I.; Foresti, E.; Lesci, I. G.; Roveri, N.; Zuccheri, T.; Scolaro, L. M. Self-Organizing Functional Materials via Ionic Self Assembly: Porphyrins H- and J-Aggregates on Synthetic Chrysotile Nanotubes. *J. Am. Chem. Soc.* **2009**, *131*, 6920−6921.

(42) Collini, E.; Ferrante, C.; Bozio, R. Strong Enhancement of the Two-Photon Absorption of Tetrakis(4-Sulfonatophenyl)porphyrin Diacid in Water upon Aggregation. *J. Phys. Chem. B* **2005**, *109*, 2−5.

(43) Collins, K. D. Charge Density-Dependent Strength of Hydration and Biological Structure. *Biophys. J.* **1997**, *72*, 65.

(44) Marcus, Y. Effect of Ions on the Structure of Water: Structure Making and Breaking. *Chem. Rev.* **2009**, *109*, 1346−1370.

(45) Bakker, H. J. Structural Dynamics of Aqueous Salt Solutions. *Chem. Rev.* **2008**, *108*, 1456−1473.

(46) Müller, K. J.; Hertz, H. G. A Parameter as an Indicator for Water-Water Association in Solutions of Strong Electrolytes. *J. Phys. Chem.* **1996**, *100*, 1256−1265.

(47) Mooney, B. L.; Corrales, L. R.; Clark, A. E. Novel Analysis of Cation Solvation Using a Graph Theoretic Approach. *J. Phys. Chem. B* **2012**, *116*, 4263−4275.

(48) Kim, J. S.; Wu, Z.; Morrow, A. R.; Yethiraj, A.; Yethiraj, A. Self-Diffusion and Viscosity in Electrolyte Solutions. *J. Phys. Chem. B* **2012**, *116*, 12007−12013.

(49) Koneshan, S.; Rasaiah, J. C.; Lynden-Bell, R. M.; Lee, S. H. Solvent Structure, Dynamics, and Ion Mobility in Aqueous Solutions at 25 C. *J. Phys. Chem. B* **1998**, *102*, 4193−4204.

(50) Collings, P. J.; Gibbs, E. J.; Starr, T. E.; Vafek, O.; Yee, C.; Pomerance, L. A.; Pasternack, R. F. Resonance Light Scattering and Its Application in Determining the Size, Shape, and Aggregation Number for Supramolecular Assemblies of Chromophores. *J. Phys. Chem. B* **1999**, *103*, 8474−8481.

(51) Micali, N.; Mallamace, F.; Castriciano, M.; Romeo, A.; Monsú Scolaro, L. Separation of Scattering and Absorption Contributions in UV/Visible Spectra of Resonant Systems. *Anal. Chem.* **2001**, *73*, 4958−4963.

(52) Knapp, E. W. Lineshapes of Molecular Aggregates. Exchange Narrowing and Intersite Correlation. *Chem. Phys.* **1984**, *85*, 73−82.

(53) Walczak, P. B.; Eisfeld, A.; Briggs, J. S. Exchange Narrowing of the J Band of Molecular Dye Aggregates. *J. Chem. Phys.* **2008**, *128*, 044505.

(54) Maiti, N. C.; Mazumdar, S.; Periasamy, N. J-and H-Aggregates of Porphyrin-Surfactant Complexes: Time-Resolved Fluorescence and Other Spectroscopic Studies. *J. Phys. Chem. B* **1998**, *102*, 1528−1538.

(55) Ogawa, T.; Tokunaga, E.; Kobayashi, T. Giant Electrooptic Response of Excitons in Porphyrin J-Aggregates. *Chem. Phys. Lett.* **2005**, *410*, 18−23.

(56) Parkash, J.; Robblee, J. H.; Agnew, J.; Gibbs, E.; Collings, P.; Pasternack, R. F.; de Paula, J. C. Depolarized Resonance Light Scattering by Porphyrin and Chlorophyll a Aggregates. *Biophys. J.* **1998**, *74*, 2089−2099.

(57) Gandini, S. C. M.; Gelamo, E. L.; Itri, R.; Tabak, M. Small Angle X-Ray Scattering Study of Meso-Tetrakis (4-Sulfonatophenyl) Porphyrin in Aqueous Solution: A Self-Aggregation Model. *Biophys. J.* **2003**, *85*, 1259−1268.

(58) Didraga, C.; Klugkist, J. A.; Knoester, J. Optical Properties of Helical Cylindrical Molecular Aggregates: The Homogeneous Limit. *J. Phys. Chem. B* **2002**, *106*, 11474−11486.

(59) Didraga, C.; Knoester, J. Optical Spectra and Localization of Excitons in Inhomogeneous Helical Cylindrical Aggregates. *J. Chem. Phys.* **2004**, *121*, 10687.

(60) Eisele, D. M.; Arias, D. H.; Fu, X.; Bloemsma, E. A.; Steiner, C. P.; Jensen, R. A.; Rebentrost, P.; Eisele, H.; Tokmakoff, A.; Lloyd, S.; et al. Robust Excitons Inhabit Soft Supramolecular Nanotubes. *Proc. Natl. Acad. Sci. U. S. A.* **2014**, *111*, E3367−E3375.

(61) Spano, F. C.; Clark, J.; Silva, C.; Friend, R. H. Determining Exciton Coherence from the Photoluminescence Spectral Line Shape in poly(3-Hexylthiophene) Thin Films. *J. Chem. Phys.* **2009**, *130*, 074904.

(62) Jagoda-Cwiklik, B.; Vácha, R.; Lund, M.; Srebro, M.; Jungwirth, P. Ion Pairing as a Possible Clue for Discriminating between Sodium and Potassium in Biological and Other Complex Environments. *J. Phys. Chem. B* **2007**, *111*, 14077−14079.

(63) Shao, Q.; He, Y.; Jiang, S. Molecular Dynamics Simulation Study of Ion Interactions with Zwitterions. *J. Phys. Chem. B* **2011**, *115*, 8358−8363.

(64) Ganguly, P.; Hajari, T.; van der Vegt, N. F. A. Molecular Simulation Study on Hofmeister Cations and the Aqueous Solubility of Benzene. *J. Phys. Chem. B* **2014**, *118*, 5331−5339.